Time-resolved angiography with stochastic trajectories for dynamic contrast-enhanced MRI in head and neck cancer: Are pharmacokinetic parameters affected?

Rafal Panek, Maria A. Schmidt,[a] and Marco Borri
CR-UK Cancer Imaging Centre, London SM2 5PT, United Kingdom; The Institute of Cancer Research, London SM2 5PT, United Kingdom; and The Royal Marsden NHS Trust, London SM2 5PT, United Kingdom

Dow-Mu Koh
The Institute of Cancer Research, London SM2 5PT, United Kingdom and The Royal Marsden NHS Trust, London SM2 5PT, United Kingdom

Angela Riddell
The Royal Marsden NHS Trust, London SM2 5PT, United Kingdom

Liam Welsh and Alex Dunlop
The Institute of Cancer Research, London SM2 5PT, United Kingdom and The Royal Marsden NHS Trust, London SM2 5PT, United Kingdom

Ceri Powell
The Institute of Cancer Research, London SM2 5PT, United Kingdom

Shreerang A. Bhide, Christopher M. Nutting, Kevin J. Harrington, and Kate L. Newbold
The Institute of Cancer Research, London SM2 5PT, United Kingdom and The Royal Marsden NHS Trust, London SM2 5PT, United Kingdom

Martin O. Leach
CR-UK Cancer Imaging Centre, London SM2 5PT, United Kingdom; The Institute of Cancer Research, London SM2 5PT, United Kingdom; and The Royal Marsden NHS Trust, London SM2 5PT, United Kingdom

(Received 7 April 2016; revised 26 September 2016; accepted for publication 30 September 2016; published 18 October 2016)

Purpose: To investigate the effects of different time-resolved angiography with stochastic trajectories (TWIST) k-space undersampling schemes on calculated pharmacokinetic dynamic contrast-enhanced (DCE) vascular parameters.
Methods: A digital perfusion phantom was employed to simulate effects of TWIST on characteristics of signal changes in DCE. Furthermore, DCE-MRI was acquired without undersampling in a group of patients with head and neck squamous cell carcinoma and used to simulate a range of TWIST schemes. Errors were calculated as differences between reference and TWIST-simulated DCE parameters. Parametrical error maps were used to display the averaged results from all tumors.
Results: For a relatively wide range of undersampling schemes, errors in pharmacokinetic parameters due to TWIST were under 10% for the volume transfer constant, K^{trans}, and total extracellular extravascular space volume, V_e. TWIST induced errors in the total blood plasma volume, V_p, were the largest observed, and these were inversely dependent on the area of the fully sampled k-space. The magnitudes of errors were not correlated with K^{trans}, V_p and weakly correlated with V_e.
Conclusions: The authors demonstrated methods to validate and optimize k-space view-sharing techniques for pharmacokinetic DCE studies using a range of clinically relevant spatial and temporal patient derived data. The authors found a range of undersampling patterns for which the TWIST sequence can be reliably used in pharmacokinetic DCE-MRI. The parameter maps created in the study can help to make a decision between temporal and spatial resolution demands and the quality of enhancement curve characterization. [http://dx.doi.org/10.1118/1.4964795]

Key words: TWIST, undersampling, DCE, squamous cell cancer of the head and neck

1. INTRODUCTION

View-sharing techniques allow for significant reduction of acquisition time, enabling fast high-resolution measurements without compromising anatomical coverage. Such techniques are often used in cardiac function examinations,[1,2] angiography,[3] flow and perfusion imaging,[4–7] and situations where breath-holds are required.[8,9] View-sharing methods employ partial k-space updating with assumptions of *a priori* knowledge to recover spatial resolution[10–13] or coverage

loss.[14] Usually, it is possible to vary the density of sampling in order to match acquisition parameters with clinical temporal and spatial redundancy (e.g., respiratory or cardiac motion and vascular input function), and thus, reduce errors. In the case of time-resolved angiography with stochastic trajectories (TWIST),[11] it is possible to vary the size of the central (fully sampled) and peripheral parts of k-space, together with the percentage of periphery sampled at a given acquisition time-point. In the case of 4D acquisition, the use of a small central compartment results in increased temporal resolution. This is especially beneficial for dynamic contrast-enhanced (DCE) MRI, where a high temporal resolution is required to appropriately characterize a progressive signal intensity change after injecting gadolinium-based (Gd-based) intravenous contrast.[15] Typical temporal resolution in these types of measurements is between 2 and 10 s depending on the level of perfusion, kinetic model used, and the necessity of motion compensation (i.e., breath holding or cardiac triggering). Variable flip angle 4D gradient echo sequences are commonly used in DCE-MRI to calculate longitudinal relaxation time, T_1, using a signal ratio between the proton density (low flip angle) and T_1-weighted (higher flip angle) images. T_1 relaxation time changes allow for Gd concentration calculations as a function of time.[16] The series of T_1-weighted images is usually acquired for a period of 3–10 min, allowing the characterization of uptake and washout of the contrast agent in studied tissues. Using appropriate kinetic models, the dynamics of Gd concentration can be related to vascular parameters such as the volume transfer constant between blood plasma and extracellular extravascular space (K^{trans}), the total extracellular extravascular space volume (V_e), or the total blood plasma volume (V_p). View-sharing techniques can be compatible with these methods. However, undersampling of peripheral parts of k-space may lead to impaired characterization of enhancement curves, ringing artifacts, and impaired fat suppression.[17–19]

In this study, we investigate the effects of different k-space undersampling schemes with TWIST on calculated pharmacokinetic (PK) DCE vascular parameters. High temporal resolution DCE data from a group of patients with head and neck squamous cell carcinoma (HNSCC) were used to evaluate TWIST-induced errors in K^{trans}, V_e, and V_p.

2. METHODS

MR images acquired prior to treatment in eight patients with HNSCC were used in the study. Written informed consent was obtained from all patients in this study, which was approved by the institutional review board (Royal Marsden Hospital Committee for Clinical Research) and research ethics committee (NHS REC number 10/H0801/32).

2.A. MRI protocol

DCE data acquired with a high temporal resolution without the use of TWIST were used as the ground truth reference. MRI was performed at 1.5 T (Philips Intera, Philips Medical Systems, Best, Netherlands). Patients were imaged in a 5-point thermoplastic mask and two flexible surface coils centered over the volume of interest were used. The DCE protocol included a trans-axial 3D spoiled fast gradient echo sequence (TE = 1 ms, TR = 4 ms, FOV = 256×256 mm^2, acquisition/reconstruction matrix: $112 \times 128/128 \times 128$, 10 slices, with $2 \times 2 \times 5$ mm^3 voxels, parallel imaging factor of 1.7, and partial Fourier acquisition of 60% in the anterior–posterior direction). A series of 20 proton density-weighted images (flip angle, FA = 4°) was initially acquired prior to contrast injection. This was followed by 100 T_1-weighted acquisitions (FA = 20°) obtained sequentially with 1.5 s temporal resolution. Gd contrast was injected intravenously at the start of the tenth dynamic scan as bolus through a peripherally placed cannula using an automatic injector (0.2 ml/kg body mass, 3 ml/s injection rate, Dotarem, Guerbet, France) and followed by a saline flush (20 ml at 3 ml/s).

2.B. PK modeling

Regions of interest (ROIs) were manually delineated by a radiation oncologist together with an expert MRI radiologist on T_1-weighted images at the time-point with maximum contrast concentration (e.g., 11th dynamic measurement, approximately 15 s after the start of contrast injection) for each slice, around all primary tumors and involved lymph nodes. Signal ratio between the proton density (FA = 4°) and T_1-weighted (FA = 20°) images was used to calculate T_1 relaxation time. First five images in each dynamic acquisition were excluded from analysis to ensure magnetization equilibrium. Signal from remaining 15 proton-weighted images acquired before the contrast injection was averaged in order to reduce the potential influence of incidental motion (i.e., due to swallowing). Changes of T_1 were used for Gd concentration calculations as a function of time, used in the PK modeling. The gadolinium contrast onset (~10th dynamic) time was manually adjusted for each DCE session. The data were analyzed using the software package MRIW (Institute of Cancer Research, UK)[20] with the extended Kety model[21] and a population-based arterial input function (AIF).[22] A set of parameters was derived including: K^{trans}, V_e, and V_p. DCE maps were produced for each parameter and lesion ROI.

2.C. Numerical DCE phantom

A digital perfusion phantom[23] was employed to simulate effects of TWIST undersampling on characteristics of signal changes in DCE-MRI using MATLAB (Mathworks, Cambridge MA). The extended Kety model was used to generate enhancement curves for K^{trans} in a range of 0.125–0.7 min^{-1} (fixed $V_e = 0.25$, $V_p = 0.01$), V_e in a range of 0.125–0.7 ($K^{\text{trans}} = 0.25$, $V_p = 0.01$), V_p in a range of 0.03–0.2 ($K^{\text{trans}} = 0.25$, $V_e = 0.25$), and temporal resolution of 0.5 s. Simulated homogenous lesions (radius = 3 pixels) were positioned along the phantom perimeter and a set of 300 simulated images (128×128 pixels) was generated.

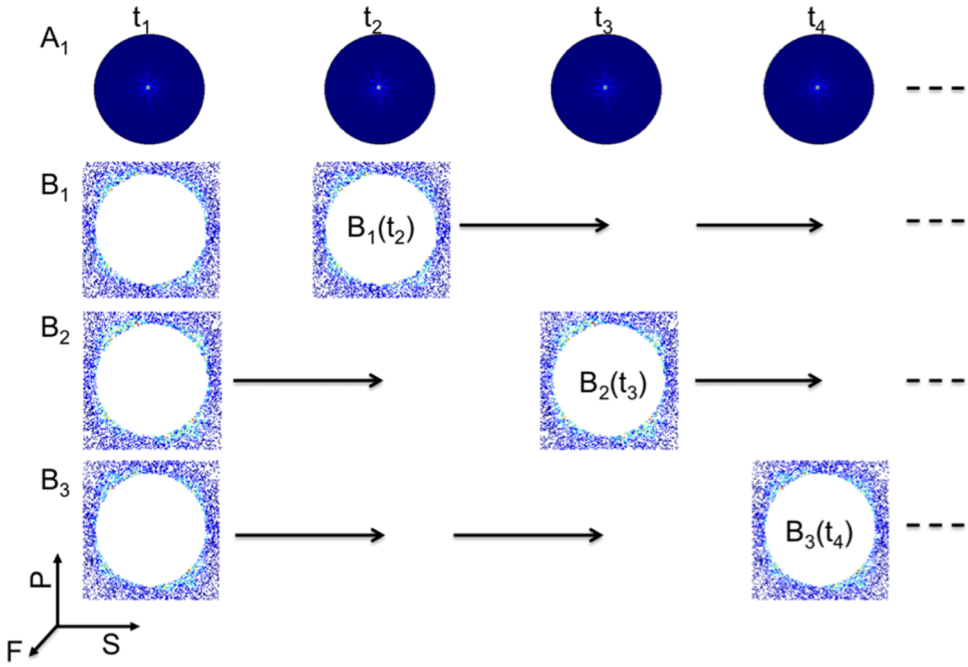

FIG. 1. TWIST acquisition scheme for $A = 50\%$ and $B = 33\%$ (P—phase encoding, F—frequency encoding, and S—partition/slice direction): k-space was divided into central (A_1) and 3 peripheral parts ($B_{1–3}$). In the first acquisition (t_1), the full k-space [$A_1(t_1)$, $B_1(t_1)$, $B_2(t_1)$, $B_3(t_1)$] was sampled. In the next acquisition, only the central $A_1(t_2)$ and 33% of peripheral $B_1(t_2)$ parts of the k-space were sampled and the missing data of $B_{2–3}(t_2)$ copied from adjacent time point t_1: $B_{2–3}(t_2) = B_{2–3}(t_1)$. Similarly, in the following acquisition steps, all points in compartment A and a percentage of the points in compartment B were sampled, with missing portions of B copied from adjacent time points.

2.D. TWIST simulations

A set of images measured or generated at each DCE time-point was Fourier transformed to obtain k-space data using MATLAB. Each k-space data set was divided into central and peripheral parts (Fig. 1). Five different areas of the central part ($A = 2\%$, 10%, 20%, 33%, and 50%) were considered. The peripheral part was subsequently undersampled, such that a defined percentage of remaining k-space points ($B = 10\%$, 33%, and 50%) was randomly sampled. For each image, all points in compartment A and a percentage of the points in compartment B were used, with missing portions of B copied from adjacent time points.

Created k-spaces were Fourier transformed to obtain a set of simulated TWIST images used for DCE pharmacokinetic calculations (Fig. 2). This approach is similar to that used

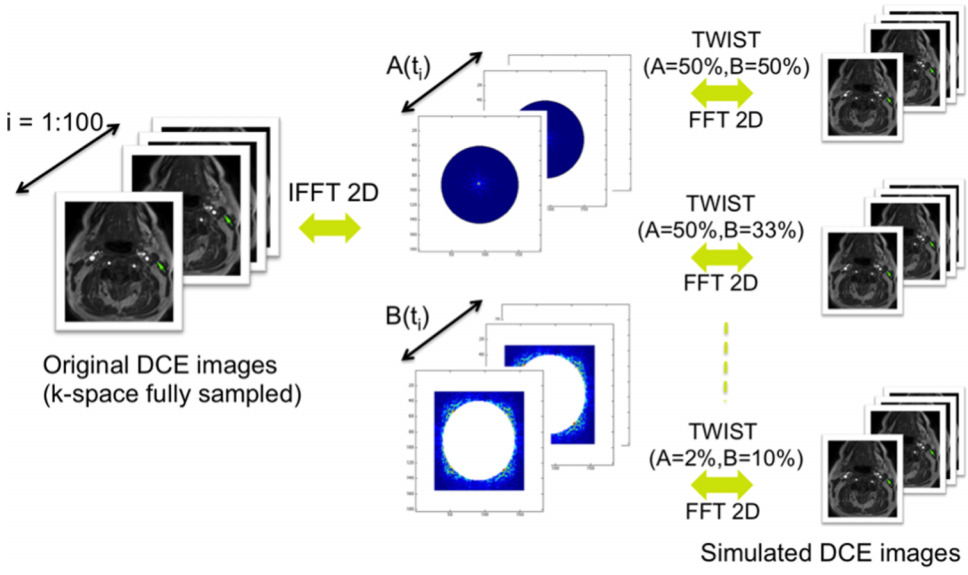

FIG. 2. Schematic diagram of TWIST simulation: fully sampled magnitude image sets were Fourier transformed to obtain k-space data. Five different sizes of the central part ($A = 2\%$, 10%, 20%, 33%, and 50%) were considered. The compartment A was fully sampled while B was sampled with reduced density ($B = 10\%$, 33%, and 50%) with missing portions of B copied from preceding time points. Simulated k-spaces were Fourier transformed to obtain a set of TWIST images used for DCE calculations.

by Song *et al.* in a simulated renography phantom study.[17] Ratios of TWIST undersampled and fully sampled reference acquisition times (TA_{TW}) were calculated for different TWIST combinations.

2.E. Error calculation for DCE parameters

In order to determine the magnitude of K^{trans}, V_e, and V_p errors, sets of DCE TWIST images were simulated for the digital phantom and every patient, with various TWIST parameter combinations. Absolute errors were calculated as a difference between measured fully sampled reference (DCE_{ref}) and TWIST-simulated (DCE_{TWIST}) DCE parameters on a pixel-by-pixel basis,

$$DCE_{error}(x,y) = |DCE_{TWIST}(x,y) - DCE_{ref}(x,y)|, \quad (1)$$

where x and y are given pixel coordinates. The percentage errors were than calculated as follows:

$$DCE_{\%error}(x,y) = \frac{DCE(x,y)_{error}}{DCE(x,y)_{ref}} * 100\%. \quad (2)$$

The median percentage difference was calculated for all voxels within each patient ROI ($n = 8$) and for 15 simulated A/B combinations ($A = 2\%$, 10%, 20%, 33%, 50% and $B = 10\%$, 33%, 50%). In the case of the phantom simulations, 12 TWIST combinations ($A = 10\%$, 20%, 33%, 50% and $B = 20\%$, 33%, 50%) were used and the results were presented in Table I. In the next step, the TWIST error distribution was studied for the whole group of patients. The results obtained for patient ROIs were averaged for each undersampling pattern and the results also presented in the form of parametrical TWIST error maps. Standard deviations (SDs) of the TWIST parameter errors were calculated and also reported in the form of parametrical maps, allowing for the assessment of intrapatient variability of parameter errors.

Kendall's tau (τ)[24] was used to test for correlations between K^{trans}, V_e, V_p, and corresponding percentage errors for all voxels. The null hypothesis stated that there was no correlation between measured DCE parameters and percentage errors. The strength of correlation was tested[24] and was considered significant if $p < 0.01$. Statistical analysis was performed using the MATLAB Statistics Toolbox.

3. RESULTS

3.A. Phantom simulations

The effect of TWIST on DCE parametrical maps simulated for $A,B = 20\%,20\%$ is presented in Fig. 3. Relatively high k-space undersampling results in blurring and ringing artifacts. DCE TWIST error maps are presented in Table I. The error magnitudes depended on the choice of undersampling pattern, parameter type, and its value. The highest errors were observed for V_p (max error 30%) and the smallest for K^{trans}, with errors below 15% for all measured values. There was a pronounced increase of error for $A < 33\%$, whereby the error increased with the value of the DCE parameter.

TABLE I. Numerical DCE phantom: TWIST errors (%) measured for various A,B combinations and DCE parameter ranges: K^{trans}: 0.125–0.7 min^{-1} (fixed $V_e = 0.25$, $V_p = 0.01$), V_e: 0.125–0.7 ($K^{trans} = 0.25$, $V_p = 0.01$), and V_p: 0.03–0.2 ($K^{trans} = 0.25$, $V_e = 0.25$).

	K^{trans}				
A,B (%)	0.125	0.25	0.4	0.55	0.7
50,50	5	1	1	1	2
50,33	5	1	3	1	1
50,20	5	1	2	1	2
33,50	4	1	2	1	1
33,33	5	1	3	1	1
33,20	4	7	9	9	8
20,50	3	9	11	17	19
20,33	6	5	5	7	5
20,20	5	5	5	8	4
10,50	2	1	1	4	7
10,33	2	2	4	4	4
10,20	2	1	2	3	6
	V_e				
	0.125	0.25	0.4	0.55	0.7
50,50	1	1	2	1	1
50,33	0	0	1	3	1
50,20	1	0	2	2	1
33,50	0	0	2	1	1
33,33	16	9	8	4	5
33,20	1	1	1	2	3
20,50	4	8	10	8	12
20,33	3	5	7	5	8
20,20	4	5	5	5	7
10,50	3	3	8	1	6
10,33	3	3	5	1	4
10,20	3	2	5	1	5
	V_p				
	0.03	0.06	0.1	0.15	0.2
50,50	3	1	2	1	2
50,33	4	3	1	1	4
50,20	4	1	1	1	3
33,50	3	3	1	1	3
33,33	4	2	1	1	3
33,20	8	13	20	25	29
20,50	3	4	11	8	29
20,33	1	2	6	6	5
20,20	2	1	8	5	6
10,50	1	1	5	3	1
10,33	3	1	3	3	2
10,20	1	1	4	3	1

3.B. Clinical simulations

Patient characteristics and tumor stages are summarized in Table II. The results for TWIST DCE parameter errors are presented in Table III. For all lesion ROIs and patients without the use of TWIST, the median values of the parameters K^{trans}, V_e, and V_p were 0.194 (SD = 0.09) min^{-1}, 0.223 (SD = 0.12), and 0.022 (SD = 0.012), respectively. DCE errors depended on the choice of undersampling pattern and varied between parameter types.

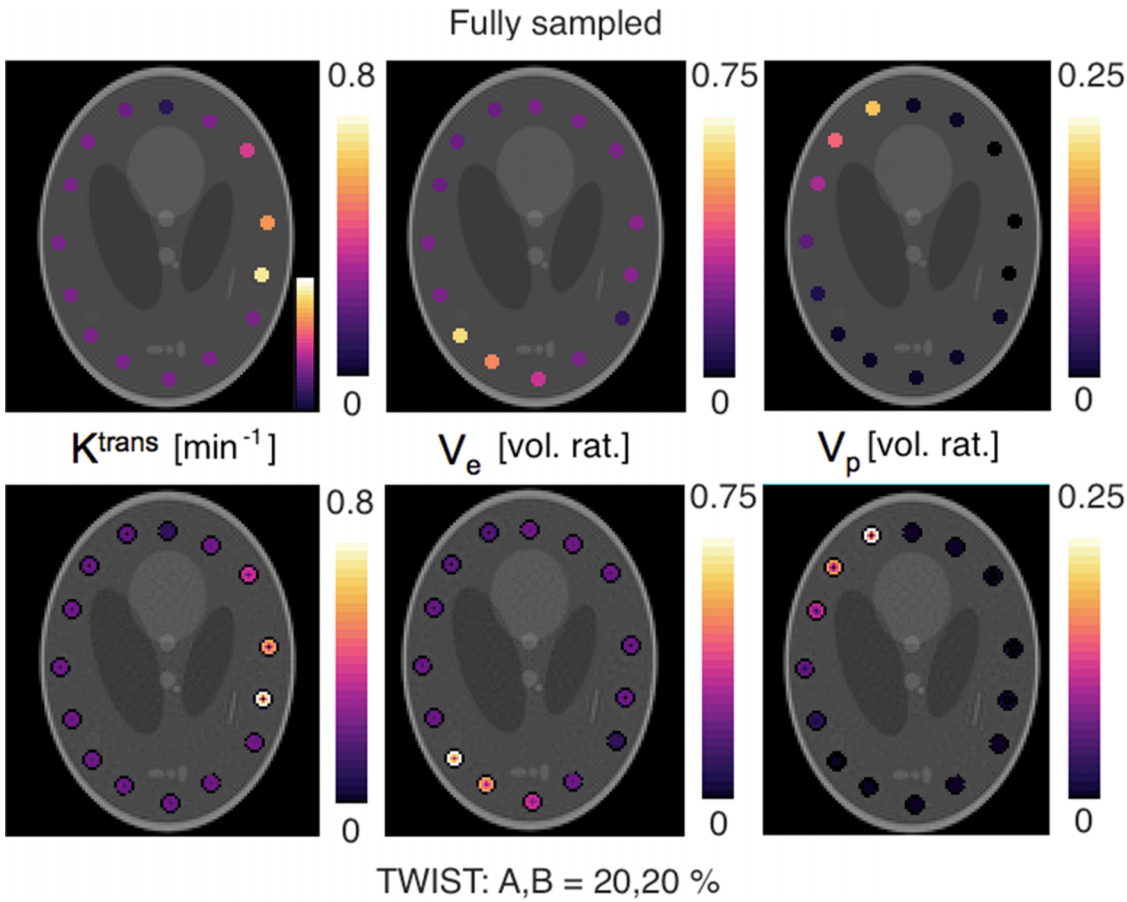

FIG. 3. Numerical DCE phantom: K^{trans}, V_e, and V_p maps calculated for a fully sampled (top) and TWIST $A,B = 20\%,20\%$ undersampled data. Simulated homogenous lesions with varying K^{trans}, V_e, and V_p were positioned along the phantom perimeter.

Median TWIST percentage error maps (HNSCC patients) are presented in Fig. 4. The K^{trans} and V_e differences were under 10% for a relatively wide range of undersampling schemes: $A > 30\%$ and $B > 20\%$. TWIST had the largest effect on the V_p parameter, where differences lower than 15% were only achieved using less extensive view-sharing parameters of $A > 35\%$ with an extended region between B: 25–35 and $A > 25\%$.

Intrapatient variability of the K^{trans} error was greater for small A and B with error standard deviation >5% for TWIST parameters A and $B < 25\%$. Standard deviations of total extracellular extravascular space volume errors were generally higher (max SD = 10%) than K^{trans} for all TWIST schemes. The variability of plasma volume errors was higher for small B values with a steep increase at $B < 20\%$.

There was no significant correlation (median $\tau = -0.12$, $p = 0.09$) observed between the K^{trans} values calculated for all measured voxels and corresponding TWIST percentage errors for all undersampling regimes used. Similarly, there was no correlation for V_p (median $\tau = 0.09$, $p = 0.11$) and a weak, statistically significant, negative correlation (median $\tau = -0.16$, $p < 0.001$) for V_e parameters and measured percentage errors. There was also no correlation between tumor ROI size and TWIST percentage errors (K^{trans} $\tau = 0.35$, $p = 0.28$; V_e: $\tau = -0.29$, $p = 0.4$, V_p: $\tau = 0.14$, $p = 0.55$).

TABLE II. Summary of patient characteristic. N/A = not available.

Patient	Age	Sex	TNM	Primary site	HPV status
1	56	M	T2N2cM0	Oropharynx	Positive
2	43	M	T1N2cM0	Nasopharynx	N/A
3	62	M	T4N2bM0	Oropharynx	N/A
4	59	M	T3N2bM0	Oropharynx	Positive
5	51	M	T1N2bM0	Hypopharynx	Negative
6	52	M	T2N2bM0	Oropharynx	Positive
7	63	F	T3N2bM0	Oropharynx	Negative
8	62	M	T3N1M0	Hypopharynx	Negative

4. DISCUSSION

The high temporal resolution of the conventional 3D gradient echo sequence allows for reliable calculations of DCE parameters. However, short acquisition times are achieved at a cost of decreased spatial resolution or volume coverage, which can lead to significant partial volume effects. This can be problematic in the case of longitudinal DCE measurements during a course of treatment, where decreasing tumor volume in responding lesions may cause the number of viable tumor voxels to become limited. Limited superior/inferior lesion coverage can also be troublesome in HNSCC where local

TABLE III. TWIST DCE parameter errors, ROI sizes, and acquisition time ratios (TA_{TW}) for all patients and undersampling combinations.

A,B (%)		50,50	50,33	50,10	33,50	33,33	33,10	20,50	20,33	20,10	10,50	10,33	10,10	02,50	02,33	02,10
	TA_{TW}	0.75	0.67	0.55	0.67	0.55	0.40	0.60	0.46	0.28	0.55	0.40	0.19	0.51	0.34	0.12
Pt No.	ROI (pixels)	Error (%): K^{trans}														
1	57	2.3	1.6	1.3	4.4	5.7	6.6	5.0	6.4	10.3	4.8	5.1	14.1	6.9	4.1	29.9
2	46	6.7	4.8	4.9	5.8	4.8	3.6	5.5	4.8	4.2	5.4	4.7	6.4	5.2	4.7	4.9
3	197	8.5	9.6	9.6	8.1	9.5	14.7	8.3	9.7	15.5	9.0	10.1	13.7	10.3	11.1	5.6
4	118	2.7	2.7	2.6	4.4	4.3	3.6	5.3	5.5	3.8	6.0	6.8	3.7	7.9	5.1	4.3
5	54	6.6	6.3	5.3	6.9	8.0	6.1	6.7	9.2	7.3	6.3	10.4	9.2	5.9	7.5	6.6
6	334	8.2	8.5	1.8	8.3	11.4	6.5	9.5	13.6	10.8	11.6	15.9	16.2	16.3	17.6	19.0
7	288	8.0	8.0	2.2	5.4	7.2	6.4	4.8	9.7	8.6	8.3	9.1	13.0	10.0	6.5	5.0
8	96	2.9	4.3	4.7	6.6	8.9	6.8	3.8	8.8	9.4	5.0	8.4	5.5	6.5	7.7	8.0
Mean	***149***	***5.7***	***5.7***	***4.1***	***6.2***	***7.5***	***6.8***	***6.1***	***8.5***	***8.7***	***7.1***	***8.8***	***10.2***	***8.6***	***8.0***	***10.4***
SD	***112***	***2.7***	***2.8***	***2.7***	***1.5***	***2.5***	***3.5***	***1.9***	***2.8***	***3.8***	***2.4***	***3.6***	***4.7***	***3.6***	***4.5***	***9.2***
Pt No.	(Pixels)	Error (%): V_e														
1	57	4.6	4.8	5.6	6.7	4.7	6.8	6.0	4.1	9.6	3.2	3.0	14.2	4.7	3.4	19.3
2	46	19.2	20.6	20.8	27.1	17.5	22.3	27.6	14.6	18.1	23.1	11.1	8.5	14.1	10.5	11.3
3	197	4.6	3.7	3.3	3.2	3.5	14.8	3.5	4.0	15.4	5.1	5.1	8.7	8.1	8.5	7.3
4	118	2.0	2.0	1.9	3.2	2.5	3.0	3.6	2.8	3.3	3.7	3.1	3.0	4.0	3.2	3.3
5	54	7.6	15.8	15.0	17.3	10.7	12.9	8.2	10.6	13.6	8.9	5.1	11.1	11.0	8.0	14.6
6	334	13.5	11.7	14.7	7.1	11.2	19.6	7.3	9.2	19.6	17.2	8.4	7.9	15.0	8.1	10.5
7	288	4.5	5.2	4.2	7.6	5.6	8.6	3.5	5.4	12.5	5.7	8.5	7.3	5.4	4.4	7.8
8	96	4.9	4.6	3.2	9.5	6.6	10.1	7.3	6.8	11.2	6.1	7.7	8.8	8.6	6.4	10.1
Mean	***149***	***7.6***	***8.5***	***8.6***	***10.2***	***7.8***	***12.3***	***8.4***	***7.2***	***12.9***	***9.1***	***6.5***	***8.7***	***8.9***	***6.6***	***10.5***
SD	***112***	***5.8***	***6.7***	***7.1***	***8.1***	***5.0***	***6.5***	***8.0***	***4.0***	***5.1***	***7.2***	***2.9***	***3.2***	***4.2***	***2.7***	***4.9***
Pt No.	(Pixels)	Error (%): V_p														
1	57	9.2	7.8	8.4	15.1	9.7	9.0	21.6	13.4	11.8	30.6	19.6	16.9	43.9	29.0	36.8
2	46	8.2	6.5	4.9	22.4	10.7	8.8	26.5	12.6	9.5	25.0	13.6	8.1	23.2	14.9	9.9
3	197	12.1	8.8	5.9	17.6	13.9	20.0	22.5	17.9	23.9	28.5	22.4	22.2	41.3	29.6	18.1
4	118	8.9	8.3	1.8	19.3	11.8	21.6	16.5	13.1	26.2	4.0	13.3	19.4	20.0	8.1	25.9
5	8.9	8.9	7.0	4.5	18.5	12.1	8.5	25.8	12.3	8.0	26.9	18.0	10.7	33.6	21.3	23.4
6	9.0	9.0	8.8	6.2	18.8	11.0	12.6	22.9	15.9	20.1	29.0	17.4	14.1	33.5	21.6	15.8
7	7.2	7.2	7.8	7.5	19.5	16.7	21.9	19.0	14.3	27.6	14.6	17.0	22.2	30.3	20.0	22.9
8	7.3	7.3	8.8	7.6	19.2	9.4	15.3	20.4	13.8	15.0	16.3	15.3	16.3	27.3	18.6	23.8
Mean	***149***	***8.9***	***8.0***	***5.8***	***18.8***	***11.9***	***14.7***	***21.9***	***14.2***	***17.8***	***21.9***	***17.1***	***16.2***	***31.6***	***20.4***	***22.1***
SD	***112***	***1.5***	***0.9***	***2.1***	***2.0***	***2.4***	***5.8***	***3.3***	***1.9***	***7.7***	***9.3***	***3.1***	***5.1***	***8.3***	***7.0***	***7.9***

lymph nodes are a common site of metastatic disease and should be imaged together with the primary site. In the case of HNSCC, the desirable superior/inferior coverage is between 10 and 20 cm with a 20–25 cm in-plane field of view, allowing for full head and neck anatomy coverage.

There is increasing interest in the use of functional imaging for biological target volume delineation in radiotherapy treatment planning.[25,26] Identification of less well-perfused regions of the tumor is of interest, as these may reflect hypoxic subvolumes, and therefore, areas of relative radioresistance.[27,28] However, this requires not only in-plane but also through-plane high spatial resolution in order to accurately identify and delineate biological tumor subvolumes, which could be potentially used for a local dose boosting. Confidence in the coregistration of radiotherapy dosimetric data and DCE parameters is particularly important where steep dose gradients exist between target volumes and surrounding healthy tissue. This could be further improved, thanks to the recent development of MR-based RT planning[29] and development of MR-Linac.[30]

The use of TWIST can overcome these limitations of conventional 3D gradient-echo techniques by increasing the user's ability to find a good compromise between coverage, temporal, and spatial resolution.

We demonstrated the influence of the TWIST view-sharing technique on DCE calculations using a digital phantom and heterogeneous groups of primary and nodal tumor sites. The use of simulated phantom data enabled the generation of reference DCE data not influenced by a limited temporal resolution and for a wide range of vascular parameters (K^{trans}, V_e, and V_p). We found that the plasma volume was the most significantly affected parameter by the TWIST undersampling, which can be explained by a dependence of V_p on the initial Gd uptake peak. K^{trans} and V_e parameter errors were below 10% for a wide range of TWIST combinations and K^{trans} and V_e values, as presented in Table I. The data

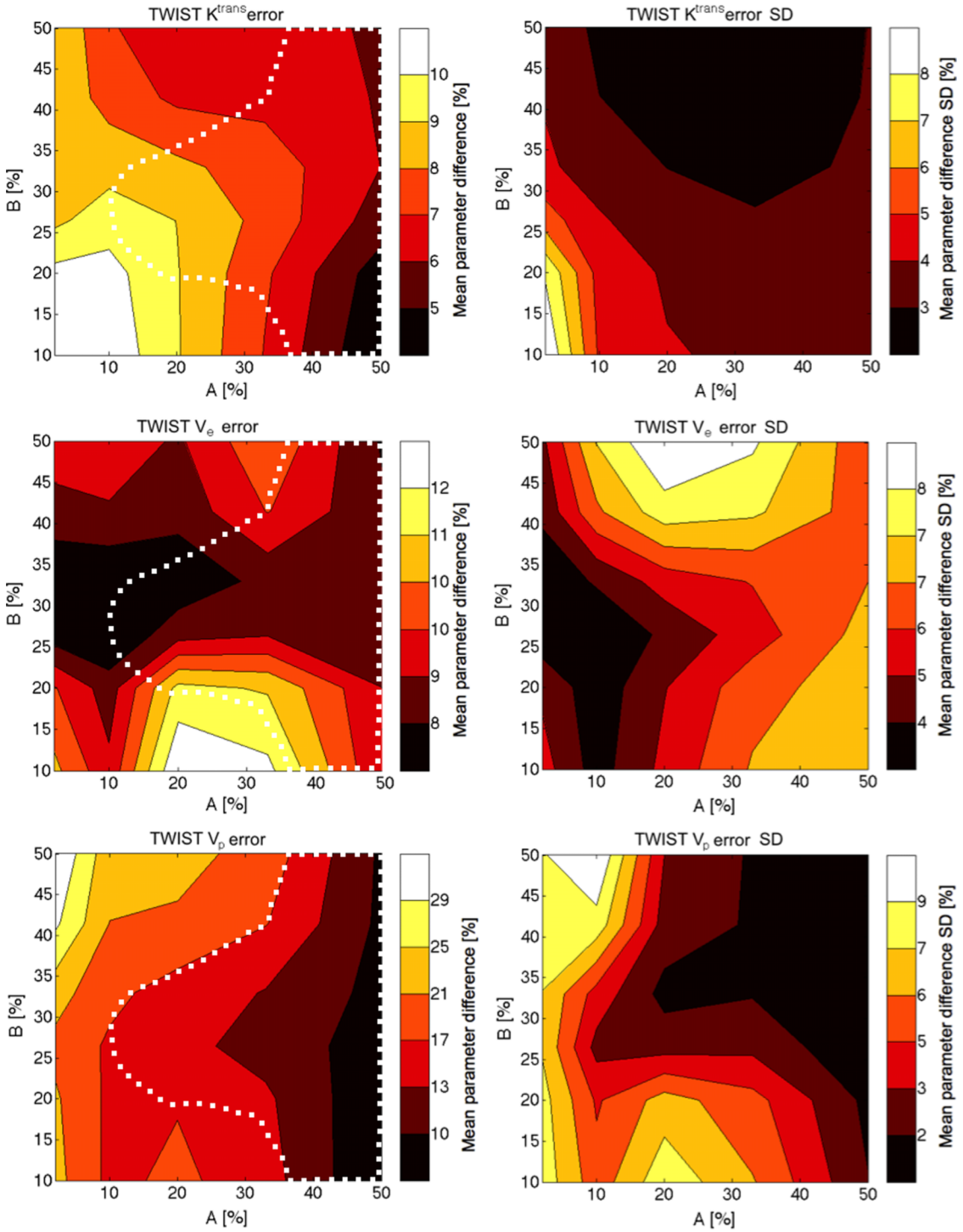

FIG. 4. TWIST parameter error maps–clinical results. An absolute value of mean percentage difference of K^{trans}, V_e, and V_p calculated using reference (no TWIST) and simulated TWIST DCE image sets is shown on the left. The white iso-contours indicate areas of all K^{trans}, V_e, and V_p errors below 15%. Standard deviations for the percentage differences are shown on the right. Simulated TWIST undersampling partition sizes: $A = 2\%$, 10%, 20%, 33%, 50% and $B = 10\%$, 33%, 50%).

suggest that it is possible to achieve errors below 15% in all K^{trans}, V_e, and V_p parameters for $A > 20\%$ and V_p below 0.1, which is expected in HNSCC (median $V_p = 0.022 \pm 0.012$ in this study).

Error maps created for various undersampling schemes can help to assist in the choice of TWIST parameters to be applied for DCE studies. For example, it would be possible to improve the spatial resolution of the DCE experimental protocol used in this study from $2\times2\times5$ mm^3 to $2\times2\times2.75$ mm^3 employing $A,B = 33\%,33\%$ TWIST undersampling, maintaining high temporal resolution (1.5 s) and coverage. In this case, the predicted TWIST induced errors would be below 10% for K^{trans}, V_e and under 15% for the V_p. The resulting spatial resolution is in line with routine radiotherapy treatment plans

taking into consideration patient positioning, motion-related uncertainties, and deliverable treatment beam geometry.[31]

The potential detrimental effects of view-sharing methods on MRI image quality were recognized before. Most studies however focused on qualitative assessment of clinical images[17–19] with few performing a quantitative analysis of dynamic signal errors.[32,33] The majority of these studies employed the "keyhole" method, which is an extreme case of view-sharing, where only the centre of k-space is updated continually, while the periphery of k-space is acquired only once at the beginning, and optionally again at the end of the dynamic series.[12] This leads to a strong geometrical dependence of dynamic signal errors and the requirement for the central k-space size to be restricted by the approximate minimum size of the expected lesion.[32] The TWIST method is less sensitive to these effects due to a sparse but continuous acquisition of peripheral part of the k-space. In our study, we do not observe correlation between lesion size and DCE TWIST errors.

One of the requirements of DCE-MRI is a requirement for a reliable measure of the AIF, representing a time course of the contrast concentration in the blood plasma pool. Patient-specific measurement of the AIF from a vessel feeding the tumor would be desirable. In practice, however, a population-based AIF is commonly used for measuring cohort and individual vascular parameters since the patient-specific repeatability is hampered by in-flow effects, nonlinear signal response, nonuniform B_1 field, pulsatile flow, and partial volume effects.[34] This approach was also adapted in this study. However, it is expected that higher temporal resolution achieved with TWIST could be beneficial in characterization of patient-specific AIF. Song *et al.*[17] found $A,B = 20\%,20\%$ TWIST sampling optimal in characterization of simulated normal and diseased kidney function (glomerular filtration rate and renal plasma flow errors $<10\%$) with one aortic input function.

Our work has several limitations. First, the k-space is obtained by Fourier transforming magnitude images, and as a consequence, phase effects on the signal are disregarded. This simulation applies either to situations where field inhomogeneity is negligible or to situations where the central portion of the k-space is sufficiently sampled to map field inhomogeneity. In a real TWIST-DCE experiment, the 3D k-space is sparsely sampled in the phase and compartment (slice) directions (Fig. 1). In our work, data are effectively undersampled in phase and readout direction and therefore is an equivalent of sagittal or coronal rather than axial 3D acquisition. Another limitation is the fact that the sampling frequency of the simulated data was constant and determined by the acquired reference DCE data. This therefore represents the use of TWIST to increase spatial resolution or coverage. This is not the case if the TWIST is used to improve temporal resolution where the sampling frequency would be higher and the induced DCE errors are likely to be lower than presented in our study. Finally, our limited patient cohort size does not represent full range of possible vascular and spatial tumor characteristics and our clinical evaluation is specific to HNSCC tumors. This was addressed to a certain extent using the digital phantom, which enabled to study TWIST effects for a wide range of DCE parameters and without temporal resolution limitations. In our work, we combined a DCE phantom with the well-known geometry (Shepp-Logan)[23] and Qualitative Imaging Biomarkers Alliance (QIBA).[35] However, a disadvantage of this approach is an arbitrary geometry of simulated enhancing lesions, the lack of spatial heterogeneity, and fixed size of regions of interest. As a consequence, the TWIST error magnitude can be elevated for particular undersampling patterns, for which effects of spatial blurring and compromised edge encoding populate significant subvolumes of simulated ROIs. This could explain higher errors calculated with $A = 20\%$, when compared to $A = 10\%$. The main advantage of using clinical data from Head & Neck studies is to reproduce accurately the range of spatial frequencies present in the region of interest, and thus evaluate more accurately the error introduced into pharmacokinetic parameters by the use of view sharing techniques. It also allows for an appropriate level of physiological noise influencing the quality of pharmacokinetic modeling. Despite of these shortcomings, our simulation achieves its objectives, as it eliminates an appropriate amount of information in space and time leading to distortion caused by TWIST to the PK parameters in HNSCC mapped. In our clinical simulations, we did not observe correlations between K^{trans}, V_e, V_p values, and the magnitude of error, for a heterogeneous group of tumor ROIs. This is in line with the phantom simulations showing pronounced increase of error for DCE parameters higher than those observed in the studied HNSCC patient group. Furthermore our simulations provide an evaluation of the minimum sampling requirements to keep the error level on the determination of pharmacokinetic parameters K^{trans}, V_e, and V_p under a given threshold. In the case of HNSCC tumors (median $K^{\text{trans}} = 0.194\ \text{min}^{-1}$, $V_e = 0.223$, and $V_p = 0.022$ in this study), the recommended size of the TWIST undersampling is A and $B > 20\%$. This allows achieving errors below 15% in all DCE parameters.

5. CONCLUSION

In conclusion, we demonstrated a method to validate and optimize k-space view-sharing techniques used for pharmacokinetic DCE studies in head and neck cancers. In this setting, the TWIST sequence can be used reliably for pharmacokinetic DCE-MRI using a range of under-sampling patterns. The parameter maps created in the study can be used to balance temporal and spatial resolution demands to allow optimal enhancement curve characterization.

ACKNOWLEDGMENTS

This work was undertaken at The Royal Marsden NHS Foundation Trust which received a proportion of its funding from the NHS Executive; the views expressed in this publication are those of the authors and not necessarily those of the NHS Executive. This work was supported by Cancer Research UK Programme Grant Nos. C46/A10588 and C7224/A13407. The authors also acknowledge the support of

CRUK and EPSRC to the Cancer Imaging Centre at ICR and RMH in association with MRC & Department of Health Nos. C1060/A10334 and C1060/A16464 and NHS funding to the NIHR Biomedical Research Centre and the Clinical Research Facility in Imaging. M.O.L. is an NIHR Senior Investigator.

[a]Author to whom correspondence should be addressed. Electronic mail: Maria.Schmidt@icr.ac.uk; Telphone: +44 (0)20 8661 3353; Fax: +44 (0)20 8915 6718.

[1]M. Doyle, E. G. Walsh, G. G. Blackwell, and G. M. Pohost, "Block regional interpolation scheme for k-space (BRISK): A rapid cardiac imaging technique," Magn. Reson. Med. **33**, 163–170 (1995).

[2]J. Tsao, P. Boesiger, and K. P. Pruessmann, "k-t BLAST and k-t SENSE: Dynamic MRI with high frame rate exploiting spatiotemporal correlations," Magn. Reson. Med. **50**, 1031–1042 (2003).

[3]J. S. Swan, T. J. Carroll, T. W. Kennell, D. M. Heisey, F. R. Korosec, R. Frayne, C. A. Mistretta, and T. M. Grist, "Time-resolved three-dimensional contrast-enhanced MR angiography of the peripheral vessels," Radiology **225**, 43–52 (2002).

[4]C. Brinegar, S. S. Schmitter, N. N. Mistry, G. A. Johnson, and Z. P. Liang, "Improving temporal resolution of pulmonary perfusion imaging in rats using the partially separable functions model," Magn. Reson. Med. **64**, 1162–1170 (2010).

[5]B. Jung, M. Honal, P. Ullmann, J. Hennig, and M. Markl, "Highly k-t-space-accelerated phase-contrast MRI," Magn. Reson. Med. **60**, 1169–1177 (2008).

[6]V. S. Lee, H. Rusinek, M. E. Noz, P. Lee, M. Raghavan, and E. L. Kramer, "Dynamic three-dimensional MR renography for the measurement of single kidney function: Initial experience," Radiology **227**, 289–294 (2003).

[7]J. J. van Vaals, M. E. Brummer, W. T. Dixon, H. H. Tuithof, H. Engels, R. C. Nelson, B. M. Gerety, J. L. Chezmar, and J. A. den Boer, "'Keyhole' method for accelerating imaging of contrast agent uptake," J. Magn. Reson. Imaging **3**, 671–675 (1993).

[8]B. S. Kim, K. R. Lee, and M. J. Goh, "New imaging strategies using a motion-resistant liver sequence in uncooperative patients," Biomed. Res. Int. **2014**, 1–11.

[9]H. J. Michaely, J. N. Morelli, J. Budjan, P. Riffel, D. Nickel, R. Kroeker, S. O. Schoenberg, and U. I. Attenberger, "CAIPIRINHA-Dixon-TWIST (CDT)-volume-interpolated breath-hold examination (VIBE): A new technique for fast time-resolved dynamic 3-dimensional imaging of the abdomen with high spatial resolution," Invest. Radiol. **48**(8), 590–597 (2013).

[10]F. R. Korosec, R. Frayne, T. M. Grist, and C. A. Mistretta, "Time-resolved contrast-enhanced 3D MR angiography," Magn. Reson. Med. **36**, 345–351 (1996).

[11]R. P. Lim, M. Shapiro, E. Y. Wang, M. Law, J. S. Babb, L. E. Rueff, J. S. Jacob, S. Kim, R. H. Carson, T. P. Mulholland, G. Laub, and E. M. Hecht, "3D time-resolved MR angiography (MRA) of the carotid arteries with time-resolved imaging with stochastic trajectories: Comparison with 3D contrast-enhanced bolus-chase MRA and 3D time-of-flight MRA," Am. J. Neuroradiol. **29**(10), 1847–1854 (2008).

[12]J. Tsao and S. Kozerke, "MRI temporal acceleration techniques," J. Magn. Reson. Imaging **36**(3), 543–560 (2012).

[13]R. A. Jones, O. Haraldseth, T. B. Müller, P. A. Rinck, and A. N. Oksendal, "K-space substitution: A novel dynamic imaging technique," Magn. Reson. Med. **29**(6), 830–834 (1993).

[14]T. B. Parrish and X. Hu, "Hybrid technique for dynamic imaging," Magn. Reson. Med. **44**(1), 51–55 (2000).

[15]D. G. Mitchell, "MR imaging contrast agents—What's in a name?," Magn. Reson. Imaging **7**, 1–4 (1997).

[16]E. K. Fram, R. J. Herfkens, G. A. Johnson, G. H. Glover, J. P. Karis, A. Shimakawa, T. G. Perkins, and N. J. Pelc, "Rapid calculation of T1 using variable flip angle gradient refocused imaging," Magn. Reson. Imaging **5**(3), 201–208 (1987).

[17]T. Song, A. F. Laine, Q. Chen, H. Rusinek, L. Bokacheva, R. P. Lim, G. Laub, R. Kroeker, and V. S. Lee, "Optimal k-space sampling for dynamic contrast-enhanced MRI with an application to MR renography," Magn. Reson. Med. **61**(5), 1242–1248 (2009).

[18]Y. Le, H. Kipfer, S. Majidi, S. Holz, B. Dale, C. Geppert, R. Kroeker, and C. Lin, "Application of time-resolved angiography with stochastic trajectories (TWIST)-Dixon in dynamic contrast-enhanced (DCE) breast MRI," J. Magn. Reson. Imaging **38**(5), 1033–1042 (2013).

[19]W. Hao, B. Zhao, G. Wang, C. Wang, and H. Liu, "Influence of scan duration on the estimation of pharmacokinetic parameters for breast lesions: A study based on CAIPIRINHA-Dixon-TWIST-VIBE technique," Eur. Radiol. **25**(4), 1162–1171 (2015).

[20]J. A. d'Arcy, D. J. Collins, A. R. Padhani, S. Walker-Samuel, J. Suckling, and M. O. Leach, "Informatics in radiology (infoRAD): Magnetic resonance imaging workbench: Analysis and visualization of dynamic contrast-enhanced MR imaging data," Radiographics **26**(2), 621–632 (2006).

[21]P. S. Tofts, G. Brix, D. L. Buckley, J. L. Evelhoch, E. Henderson, M. V. Knopp, H. B. Larsson, T. Y. Lee, N. A. Mayr, G. J. Parker, R. E. Port, J. Taylor, and R. M. Weisskoff, "Estimating kinetic parameters from dynamic contrast-enhanced T(1)-weighted MRI of a diffusable tracer: Standardized quantities and symbols," J. Magn. Reson. Imaging **10**(3), 223–232 (1999).

[22]M. R. Orton, J. A. d'Arcy, S. Walker-Samuel, D. J. Hawkes, D. Atkinson, D. J. Collins, and M. O. Leach, "Computationally efficient vascular input function models for quantitative kinetic modelling using DCE-MRI," Phys. Med. Biol. **53**(5), 1225–1239 (2008).

[23]R. Grimm, J. Churt, A. Fieselmann, K. T. Block, B. Kiefer, and J. Hornegger, "A digital perfusion phantom for T1-weighted DCE-MRI," Proc. Intl. Soc. Mag. Reson. Med. **20**, 2559 (2012).

[24]M. Kendall, "A new measure of rank correlation," Biometrika **30**, 81–89 (1938).

[25]K. Newbold, I. Castellano, E. Charles-Edwards, D. Mears, A. Sohaib, M. O. Leach, P. Rhys-Evans, P. Clarke, C. Fisher, K. Harrington, and C. Nutting, "An exploratory study into the role of dynamic contrast-enhanced magnetic resonance imaging or perfusion computed tomography for detection of intratumoral hypoxia in head-and-neck cancer," Int. J. Radiat. Oncol., Biol., Phys. **74**(1), 29–37 (2009).

[26]C. Powell, M. Schmidt, M. Borri, D. M. Koh, M. Partridge, A. Riddell, G. Cook, S. A. Bhide, C. M. Nutting, K. J. Harrington, and K. L. Newbold, "Changes in functional imaging parameters following induction chemotherapy have important implications for individualised patient-based treatment regimens for advanced head and neck cancer," Radiother. Oncol. **106**(1), 112–117 (2013).

[27]M. R. Horsman, L. S. Mortensen, J. B. Petersen, M. Busk, and J. Overgaard, "Imaging hypoxia to improve radiotherapy outcome," Nat. Rev. Clin. Oncol. **9**(12), 674–687 (2012).

[28]D. Thorwarth, S. M. Eschmann, F. Paulsen, and M. Alber, "Hypoxia dose painting by numbers: A planning study," Int. J. Radiat. Oncol., Biol., Phys. **68**(1), 291–300 (2007).

[29]M. A. Schmidt and G. S. Payne, "Radiotherapy planning using MRI," Phys. Med. Biol. **60**(22), R323–R361 (2015).

[30]J. J. Lagendijk, B. W. Raaymakers, A. J. Raaijmakers, J. Overweg, K. J. Brown, E. M. Kerkhof, R. W. van der Put, B. Hardemark, M. van Vulpen, and U. A. van der Heide, "MRI/linac integration," Radiother. Oncol. **86**(1), 25–29 (2008).

[31]S. H. Benedict, K. M. Yenice, D. Followill, J. M. Galvin, W. Hinson, B. Kavanagh, P. Keall, M. Lovelock, S. Meeks, L. Papiez, T. Purdie, R. Sadagopan, M. C. Schell, B. Salter, D. J. Schlesinger, A. S. Shiu, T. Solberg, D. Y. Song, V. Stieber, R. Timmerman, W. A. Tome, D. Verellen, L. Wang, and F. F. Yin, "Stereotactic body radiation therapy: The report of AAPM Task Group 101," Med. Phys. **37**(8), 4078–4101 (2010).

[32]J. E. Bishop, G. E. Santyr, F. Kelcz, and D. B. Plewes, "Limitations of the keyhole technique for quantitative dynamic contrast-enhanced breast MRI," J. Magn. Reson. Imaging **7**(4), 716–723 (1997).

[33]D. Lee, P. B. Greer, S. Pollock, T. Kim, and P. Keall, "Quantifying the accuracy of the tumor motion and area as a function of acceleration factor for the simulation of the dynamic keyhole magnetic resonance imaging method," Med. Phys. **43**(5), 2639–2648 (2016).

[34]M. Rata, D. J. Collins, J. Darcy, C. Messiou, N. Tunariu, N. Desouza, H. Young, M. O. Leach, and M. R. Orton, "Assessment of repeatability and treatment response in early phase clinical trials using DCE-MRI: Comparison of parametric analysis using MR- and CT-derived arterial input functions," Eur. Radiol. **26**(7), 1991–1998 (2016).

[35]D. Barboniak and R. Price, "Digital reference objects for dynamic contrast-enhanced MRI," QIBA Newstler **5**(1), 1 (2013).